Transition to shear-driven turbulence in Couette-Taylor flow

Daniel P. Lathrop,* Jay Fineberg, and Harry L. Swinney†
Center for Nonlinear Dynamics, University of Texas, Austin, Texas 78712
and Department of Physics, University of Texas, Austin, Texas 78712
(Received 27 March 1992)

Turbulent flow between concentric cylinders is studied in experiments for Reynolds numbers $800 < R < 1.23 \times 10^6$ for a system with radius ratio $\eta = 0.7246$. Despite predictions for the torque scaling as a power law of the Reynolds number, high-precision torque measurements reveal no Reynolds-number range with a fixed power law. A well-defined nonhysteretic transition at $R = 1.3 \times 10^4$ is marked by a change in the Reynolds-number dependence of the torque. Flow quantities such as the axial turbulent diffusivity, the time scales asociated with the fluctuations of the wall shear stress, and the root-mean-square fluctuations of the wall shear stress and its time derivative are all shown to be simply related to the global torque measurements. Above the transition, the torque measurements and observed time scales indicate a close correspondence between this closed-flow system and open-wall–bounded-shear flows such as pipe flow, duct flow, and flow over a flat plate.

PACS number(s): 47.25.Ae, 47.20.Ft, 47.25.Jn, 47.25.Ei

I. INTRODUCTION

Turbulence, although ubiquitous in nature, remains in many aspects an enigma. Most turbulence experiments are conducted in open-flow systems. Here we consider turbulence in a simple closed-flow system. At low Reynolds number the behavior of closed-flow systems is typically different from that in open-flow systems. With increasing Reynolds number many open-flow systems have a hysteretic transition from the laminar to the turbulent state, while closed-flow systems generally display an ordered sequence of bifurcations leading from laminar flow to chaos and turbulence. This raises the question of whether or not these systems also exhibit different behavior at high Reynolds number. The closed system that we have studied is flow between concentric rotating cylinders (the Couette-Taylor system). Our experiments [1] extend to Reynolds numbers well beyond those previously studied.

The Couette-Taylor system has several advantages as an experimental system. The rotation of the inner cylinder, which drives the system, is amenable to precise control. Also, because of its simple geometry and high symmetry, a Couette-Taylor system can be built to tight tolerances. These two advantages insure well-defined, reproducible experimental boundary conditions.

The Reynolds number in a system with only the inner cylinder rotating (as in our work) can be defined as

$$R = \frac{\Omega a (b-a)}{\nu} , \tag{1}$$

where Ω is the rotation rate of the inner cylinder, a and b are the radii of the inner and outer cylinders, and ν is the kinematic viscosity of the fluid. For low Reynolds numbers this system has been extensively studied [2,3] and has been found to exhibit a well-defined sequence of bifurcations leading to weak turbulence [4–6]. The seminal work of Taylor in 1923 demonstrated that the laminar Couette state undergoes a transition to an axially periodic state, Taylor vortex flow [7]. The next transition leads to a state with waves on the vortices; Coles (1965) [8] found that multiple wavy vortex flow states could be stable at a given R. Subsequent experiments have studied higher instabilities, the transition to chaos, and turbulent Taylor vortices (Fig. 1) [4–6].

The present study examines the behavior of the Couette-Taylor system at Reynolds numbers well beyond the onset of chaos. Using high-precision torque measurements, local wall shear stress measurements, and flow visualization in the Reynolds number range $800 < R < 1.23 \times 10^6$, we will demonstrate that after a well-defined transition at $R_T = 1.3 \times 10^4$, this system behaves like a wall-bounded shear flow.

The paper is organized as follows. Section II reviews previous experimental work and theoretical predictions for the torque. The experimental apparatus is described in Sec. III. Flow visualization results in Sec. IV show the small-scale structure as well as the turbulent Taylor vortices. The torque measurements are presented in Sec. V and are compared with past experiments and theory. In Sec. VI the behavior of the wall shear stress fluctuations and the turbulent diffusion measurements of Tam and Swinney are shown to be related to the torque and Reynolds number. Section VII explores the relationship of the Couette-Taylor system to wall-bounded shear flows, and Sec. VIII contains concluding remarks.

II. BACKGROUND

Couette-Taylor flow has been studied extensively at low Reynolds numbers [9], but there have been few experiments performed at high Reynolds numbers ($> 10^4$). Smith and Townsend [10,11] conducted Couette-Taylor experiments in the Reynolds number range $7.2 \times 10^3 < R < 1.2 \times 10^5$ for radius ratio $\eta \equiv a/b = 0.667$ and aspect ratio $\Gamma \equiv L/(b-a) = 23.7$, where L is the length

of the annulus. Using a hot-wire probe in air, they observed that the system possessed thin boundary layers separated by a nearly inviscid core region. The core was characterized by a mean angular momentum density $\mathcal{L}$, which was nearly constant. [$\mathcal{L}$ is the axial component of the mean angular momentum density $r\bar{u}_\theta(r)$.] In those experiments, turbulent Taylor vortices persist up to $R=4.2\times10^4$. Past this, the vortices "either disappear into fully irregular, turbulent flow or, more probably, become too fragmented or distorted to be easily distinguishable."

Kataoka *et al.* [12] also observed the breakdown of the axial periodicity in a Couette-Taylor system with $\eta=0.619$ and $\Gamma=21.1$. Using an axial array of electrochemical probes, they observed an axial periodicity in the wall shear stress showing the existence of turbulent Taylor vortices up to $R=1.2\times10^4$; for larger Reynolds number no axial periodicity was observed. Neither Smith and Townsend nor Kataoka used flow visualization methods to examine the turbulent Taylor vortices.

Wendt [13] performed the only detailed torque measurements in the Couette-Taylor system at high Reynolds numbers, which ranged from 50 to 10^5. Three different radius ratios were used, $\eta=0.680$, 0.850, and 0.935, with respective aspect ratios of $\Gamma=8.5$, 18, and 42. He fit his measurements of the nondimensional torque $G=T/\rho\nu^2L$ (where T is the torque and ρ is the fluid density) to

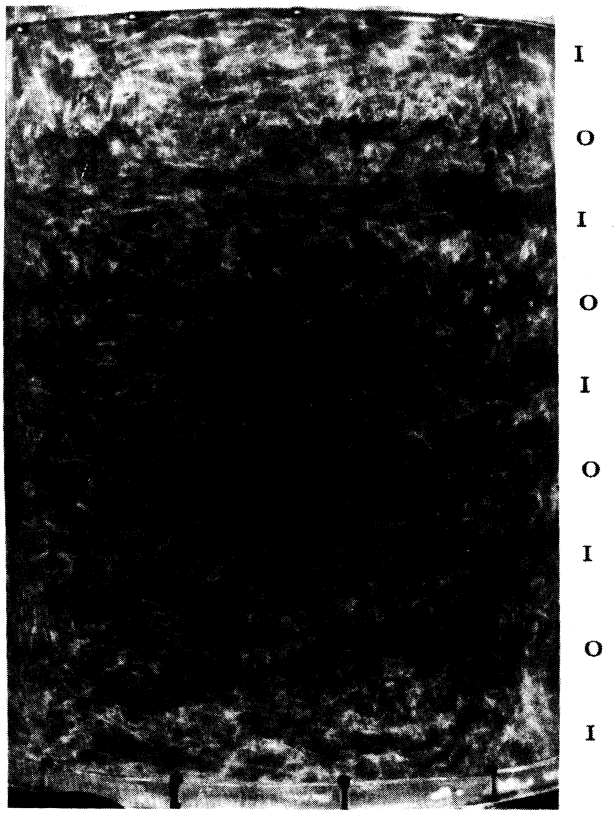

FIG. 1. Flow visualization showing turbulent Taylor vortices at $R=12\,000$, obtained using a 0.1% concentration of Kalliroscope added to the working fluid. The inflow (I) and outflow (O) boundaries are labeled.

$$G=\begin{cases}1.45\dfrac{\eta^{3/2}}{(1-\eta)^{7/4}}R^{1.5} & \text{for } 4\times10^2<R<10^4\\ 0.23\dfrac{\eta^{3/2}}{(1-\eta)^{7/4}}R^{1.7} & \text{for } 10^4<R<10^5\ ,\end{cases}\tag{2}$$

with an uncertainty of 3%. Measurements by Taylor [14] cover the same range but were not fit to any empirical expression.

Recently, measurements by Tong *et al.* [15] also reported power-law scaling $G\sim R^{1.8}$ over the range $4\times10^4<R<4\times10^5$ for $\eta=0.448$. The measurement technique there, measuring the torque from the motor power, unfortunately admits several confounding errors: efficiency losses, drag from bearings and seals, and drag from end sections. The torque data of Tong *et al.* and Wendt fit power laws well, within the errors of the given torque measurements, but with different exponents.

Observations of power-law scaling in turbulent closed-flow systems are not isolated to the Couette-Taylor system. Rayleigh-Bénard experiments performed by Castaing and co-workers [16,17] yielded power-law behavior for the Nusselt number Nu (the nondimensional heat transport) as a function of the Rayleigh number Ra (the nondimensional temperature difference across the convection cell), $\mathrm{Nu}\sim\mathrm{Ra}^\gamma$. Castaing and co-workers found a "soft turbulence" regime with scaling exponent $\gamma=\frac{1}{3}$ for $5\times10^5<\mathrm{Ra}<4\times10^7$, and for $\mathrm{Ra}>4\times10^7$, a "hard turbulence" regime with $\gamma=\frac{2}{7}$. They also observed that the probability distribution of the temperature fluctuations changed discontinuously from Gaussian below the transition to exponential above the transition. The Couette-Taylor experiments of Wendt and the Rayleigh-Bénard experiments suggest that sharp transitions can occur between distinct regimes in turbulent flow.

Malkus and Veronis [18], using a marginal stability calculation, predicted $\gamma=\frac{1}{3}$ for Rayleigh-Bénard convection. An analogous marginal stability calculation was performed by Marcus and co-workers [19,20] for the Couette-Taylor system. The calculation assumes that the gap is divided into three radial regions: two thin boundary layers, one near the inner cylinder of thickness δ_{in} and one near the outer cylinder of thickness δ_{out}, and an inviscid core separating them. The core is assumed to have a constant angular momentum density $\mathcal{L}$, an assumption supported by the measurements of Smith and Townsend [10]. The crux of the marginal stability argument is that the boundary layer thickness is maintained such that the boundary layers are laminar and marginally stable to disturbances such as Taylor vortices.

The next step in the marginal stability argument is to match the mean angular velocities where the boundary layers join to the core at $r=b-\delta_{\text{out}}$ and $r=a+\delta_{\text{in}}$. The final step is to require that the torques be equal at the inner and outer cylinders, as they must be when the fluid undergoes no net angular acceleration (in steady state). These conditions of marginal stability of each boundary layer, mean velocity matching, and equal torques, allow one to solve for the unknowns δ_{in}, δ_{out}, the mean angular momentum density $\mathcal{L}$, and the torque G. The Marcus

[19] predictions for $\eta \to 1$ can be extended to arbitrary η, yielding [21]

$$\begin{aligned} G &= 0.202(\eta^{-1}-1)^{-5/3}R^{5/3}, \\ \delta_{\text{in}}/a &= 6.32(\eta^{-1}-1)^{2/3}R^{-2/3}, \\ \delta_{\text{out}}/b &= 8.16(\eta^{-1}-1)^{2/3}R^{-2/3}, \\ \mathcal{L} &= 0.563\Omega a^2 . \end{aligned} \tag{3}$$

Similar calculations were done by Barcilon and Brindley [22], using boundary layers marginally stable to Görtler vortices, not Taylor vortices, and they obtained the same scaling of the torque $G \sim R^{5/3}$, which is not surprising since both Görtler and Taylor vortices arise due to centrifugal instability.

A power-law prediction for the torque can also be derived from a Kolmogorov-type argument [23]. We assume that the energy dissipation rate is constant within the inertial range, independent of length scale, and given by

$$\varepsilon = \frac{(\Delta U)^3}{l} , \tag{4}$$

where ε is the dissipation rate per unit mass per unit time for velocity differences ΔU across a length scale l. We apply this relation at the largest length scale $l = (b-a)$ and $\Delta U = \Omega a$. Equation (4) then yields $\varepsilon = (\Omega a)^3/(b-a)$. The torque, which is given by the total power dissipated divided by the rotation rate, follows

$$G = \pi \left[\frac{\eta(1+\eta)}{(1-\eta)^2} \right] R^2 . \tag{5}$$

This calculation is relevant in the limit of infinite Reynolds number, where the viscous effects are negligible, and thus the scaling exponent $\alpha = 2$ might be considered an upper limit. The value of 2 for α was obtained previously by Nickerson [24] and was recently derived directly from the Navier-Stokes equation by Doering and Constantin [25]. The result $\alpha = 2$ is useful in understanding the structure of the velocity fluctuations. Equation (4) predicts cube root singularities in the flow field $\Delta U = \varepsilon^{1/3} l^{1/3}$. This establishes a connection between the form of the velocity fluctuations and a scaling exponent $\alpha = 2$. Any deviations from this prediction might lead us to suppose that typical eddies also follow a different scaling law.

III. EXPERIMENTAL APPARATUS

We designed the experimental apparatus for high-precision torque measurements and flow visualization at as high a Reynolds number as was feasible in a practical table-top experiment. A cross section of the apparatus is shown in Fig. 2. The outer cylinder is cast Plexiglas [26] (polymethylmethacrylate) with inner radius $b = 22.085$ cm and a thickness of 3.34 cm. The inner surface of the outer cylinder is machined to a cylindricity tolerance of 0.023% (50 μm). After machining, the cylinder was polished until transparent [27]. The axial length of the working section is $L = 69.50$ cm. The apparatus has a stainless steel inner cylinder with radius $a = 16.000$ cm,

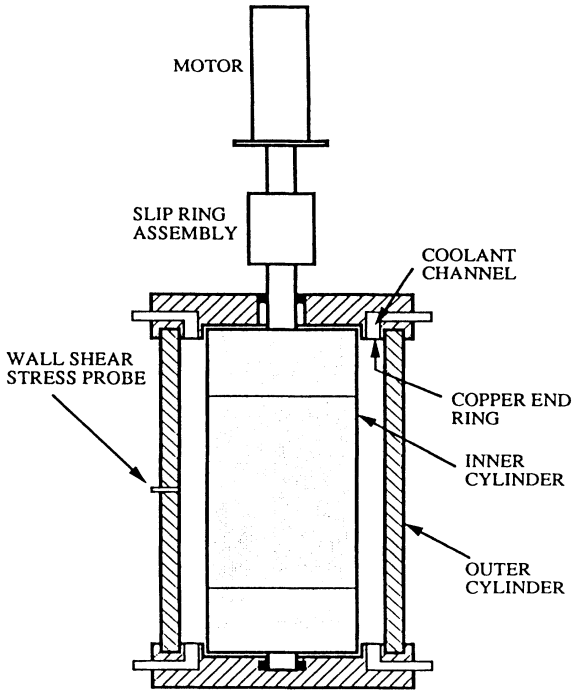

FIG. 2. The Couette-Taylor system consists of a Plexiglas outer cylinder and a stainless steel inner cylinder (see Fig. 3). Temperature control is achieved via coolant channels in each end, separated from the working fluid by thin copper rings.

giving the system a radius ratio $\eta = a/b = 0.7246 \pm 0.0001$ and an aspect ratio $\Gamma = L/(b-a) = 11.47$. The inner cylinder was machined and ground to a cylindricity tolerance of 0.016% and a root-mean-square roughness of 0.2 μm. A 2 kW Compumotor KHX-740 dc servomotor drives the inner cylinder, with an accuracy (averaged over one rotation) of 0.2% of the set speed.

The inner cylinder is constructed in three sections of length 15.69, 40.64, and 15.69 cm, stacked axially and separated by 0.03 cm gaps (see Fig. 3). The upper and lower sections are rigidly attached to the rotating drive shaft, which is directly coupled to the motor.

To minimize end effects in the torque measurements, only the center section of the inner cylinder senses torque. It is connected to the shaft via two low torque precision bearings (static torque 2 g cm each, Miniature Precision Bearings Part S3240MS07) and a torque-sensing strain arm. All of the torque passing to the center section passes through the strain arm, causing an elongation and compression of strain gauges (at most 0.1% of their length) bonded to either side of the arm. The strain arm is constructed of 2024-T4 spring aluminum. The strain gauges (Measurements Group Inc. N2A-13-T006N-350), which change their resistance with applied strain, have a combined hysteresis and creep of at most 0.02% of the maximal change in resistance, and have a temperature coefficient of 0.1%/°C. Calibration using weights hung at a known radius show linearity of the strain arm to within the precision of our measurements (0.03% of full scale).

The arrangement of the torque measurement electron-

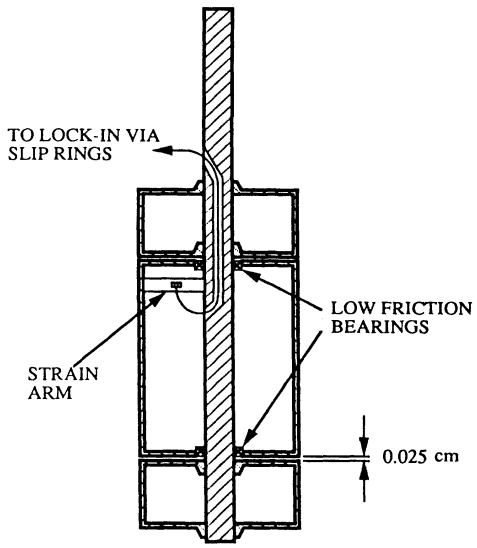

FIG. 3. The inner cylinder is divided into three segments. Only the inner section senses torque. It is suspended by low friction bearings, and all of the torque for the center section passes through a torque-sensing strain arm.

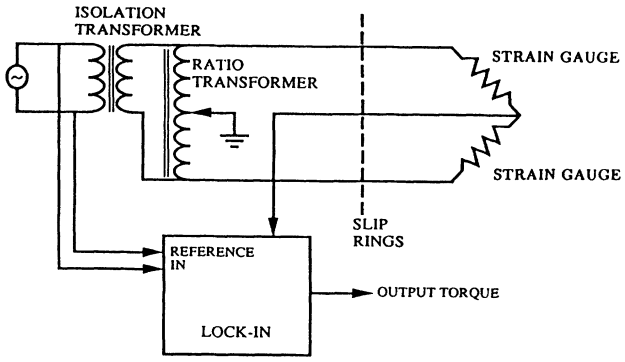

FIG. 4. Torque is measured using strain gauges mounted inside the inner cylinder. The strain gauges form half of an ac Wheatstone bridge. The bridge is completed in the nonrotating frame via a ratio transformer. The output signal from a lock-in voltmeter yields the torque value.

ics is shown in Fig. 4. The two strain gauges form half of an ac Wheatstone bridge. Slip rings are used to bring the signal outside of the rotating frame. The bridge is completed by a seven-digit Gertsch ratio transformer and is driven at 88.8 Hz through an isolation transformer. The bridge output is monitored using an Ithaco 391 lock-in detector, low-pass filtered with a 1.2 s time constant, and digitized with 12-bit resolution.

Lock-in detection of the strain gauge signal is necessary due to the large noise generated by the motor. To reduce the noise, care was taken in the placement of grounds, including a substrate ground for the strain gauges. Computer averaging the torque signal over a one minute time period increases the signal-to-noise level to 80 dB for the largest measured torque values; the smallest torque measurements that we use still have a signal-to-noise level of at least 56 dB.

To achieve the desired accuracy in the torque measurements, five different water-glycerol mixtures were used with overlapping Reynolds-numbers ranges, as summarized in Table I. In each fluid the torque was in the range 0.3–8 N m. The viscosities of the water-glycerol mixtures have a large temperature dependence (up to 7.3%/°C for the mixtures studied); hence precise temperature control was required. At the largest Reynolds number achieved, $R = 1.23 \times 10^6$, nearly 2 kW of power is dissipated in the fluid [28] and must be extracted by the temperature control system.

Heat is exchanged between a coolant fluid and the working fluid through end rings that bound the working fluid axially (see Fig. 2). The end rings are made of copper, 0.3 cm thick. The turbulent transport of passive scalars ensures that the generated heat is moved rapidly to the end rings. Even at the highest Reynolds numbers, the temperature measured with thermistor probes placed flush with the outer wall varies by less than 0.01 °C throughout the central section of the working fluid.

A pump circulates the coolant fluid from a tank past the end rings at a flow rate of 900 liter/min. The fluid coming from the tank is divided six ways, three for each end of the annulus, by special manifolds that split the flow symmetrically to minimize angular gradients. The flow is returned to the coolant tank via a similar manifold. The temperature of the working fluid is maintained to within 0.1 °C of the set point with a controller that supplies heat as needed to heating elements while a 4.5 kW refrigerator supplies cooling at a constant rate. The thermistor control sensor is mounted flush with the outer cylinder. Temperature control is much better, about 0.01 °C, for runs when the rotation rate is not varied over a large range.

Local fluctuations in the wall shear stress were measured using a hot film probe (TSI model 1268W). This probe was mounted flush with the outer cylinder to within 25 μm, in contact with the working fluid. The

TABLE I. Water and water-glycerol mixtures and their properties.

Glycerol by weight (%)	Temp. (°C)	Density (g/cm^3)	Kinematic viscosity (10^{-2}cm^2/s)	Temp. coef. of visc. (%/°C)	Max. $\Omega/2\pi$ (Hz)	Reynolds number min.	Reynolds number max.
0	30	0.996	0.80	2.3	16.5	1×10^5	1.2×10^6
35	24	1.02	2.7	3.1	14	8×10^4	6×10^5
57	24	1.07	7.6	3.6	12	2×10^4	2×10^5
70	24	1.10	18.0	5.3	10	6×10^3	7×10^4
79	24	1.20	39.0	7.3	8	8×10^2	2×10^4

sensing element of the probe is 0.030 cm azimuthally by 0.11 cm axially. The probe was run in the constant temperature mode using a TSI model 1653B anemometer. In this mode the frequency response of these probes exceeds 10 kHz [29]. The output of the constant temperature anemometer was acquired with a signal-to-noise ratio of 52 dB at rates up to 16 kHz.

The voltage V required to maintain a hot film probe at constant temperature is often described by [29]

$$V^2 = A\tau_w^{1/3} + B \ , \tag{6}$$

where the calibration constants A and B depend on fluid properties (heat capacity, thermal diffusivity, and viscosity), the temperature difference between the probe and the working fluid (commonly referred to as the overheat), the resistance of the probe, and the type and mass of the substrate. It is best to calibrate such probes *in situ* during each run. To calibrate our probes, the mean voltage from the probe was compared to the measured torque over a range of rotation rates. The torque T was used to find the mean wall shear stress at the outer cylinder $\tau_w = T/2\pi b^2 L$. The calibration constants A and B can be determined by linear regression of V^2 as a function of $\tau_w^{1/3}$. Although linear regression yields a good fit for the data, the residuals show a systematic curvature. This systematic deviation led us to use the following fit to the data:

$$V^2 = C\tau_w^{2/3} + D\tau_w^{1/3} + E \ . \tag{7}$$

The coefficients C, D, and E were calculated for each run. They deviated only slightly from run to run with the same fluid, but were quite different for unlike fluids [21].

IV. FLOW VISUALIZATION

To complement our measurements of torque and wall shear stress, we visualize the flow by introducing a 0.1% concentration of Kalliroscope [30] into the working fluid. Kalliroscope is composed of small ($\sim$ 20 μm width) flat flakes that locally align with the stream surfaces [31]. Figure 5 shows photographs of turbulent states at $R = 6.0\times10^3$, 2.4×10^4, 4.8×10^4, and 1.2×10^5, well beyond the onset of chaos ($R \sim 10^3$ [5]); see also Fig. 1, $R = 1.2\times10^4$. The smallest length scale clearly decreases with increasing Reynolds numbers. Although turbulent Taylor vortices are observed at moderate Reynolds numbers, no vortices are discernible [32] above $R \sim 10^5$. Above $R \sim 10^5$ large-scale structures are evident but do not appear to be stationary. At low Reynolds numbers we find stable states with eight, ten, and twelve vortices. With increasing Reynolds number, the twelve-vortex state becomes unstable at $R = 6\times10^3$ to the ten-vortex state, which becomes unstable at $R = 1.75\times10^4$ to the eight-vortex state. The eight-vortex state is stable until the disappearance of the vortices.

V. TORQUE

A. Measurements

The torque measurements were designed to determine the scaling exponent α in $G \sim R^{\alpha}$. Runs were made for each of the five fluids in Table I. In the overlapping Reynolds-number ranges the torque measurements for different fluids agreed within the experimental uncertainty.

Experiments were repeated several times for each fluid over the same Reynolds-number range for increasing and decreasing rotation rates. Since the torque depends on the number of vortices in the system, procedures for systematically producing a given number of vortices (using rapid accelerations and decelerations) were found and applied in the region $R < 1.75\times10^4$, where different numbers of vortices are stable. For $R < 1.75\times10^4$, the torque measurements were made on fluids containing Kalliroscope so the number of vortices could be simultaneously determined. No difference in torque was discernible in measurements with and without Kalliroscope. For $R > 1.75\times10^4$ it was not necessary to use Kalliroscope since there was no ambiguity regarding the number of vortices.

For each set of measurements, we first determined the output from the lock-in amplifier at zero torque; this provided a baseline for the torque measurements. For a given fluid, the minimum nonzero rotation rate was chosen so that the torque measurements would have a signal-to-noise ratio of 56 dB (see Sec. III). The torque was then measured at a number of rotation rates Ω_n given by $\Omega_{n+1} = 1.035\Omega_n$, which gives a uniform spacing on a logarithmic scale. After each experiment we took a fluid sample and measured its kinematic viscosity ν as a function of temperature over a 1 °C range using Cannon-Fenske Routine viscometers of sizes 50, 200, and 400 (depending on the fluid) to an accuracy of 1%. The density ρ of each fluid used was measured to an accuracy of 0.5%.

In our analysis we consider the nondimensionalized torque $G \equiv T/\rho\nu^2 L_{\text{center}}$, where T is the measured torque and L_{center} is the length of the torque-sensing inner cylinder center section. The torque measurements for the eight- and ten-vortex states are shown in Figs. 6 and 7. At small R the torque for the eight-vortex state, which has an average axial wavelength of $2.87(b-a)$, is larger than that for the ten-vortex state, which has an average axial wavelength of $2.29(b-a)$, but for $R > 3000$ the torque is larger for the ten-vortex state, as Fig. 8 shows. Measurements made for increasing and decreasing Reynolds number showed no hysteresis for either flow state.

B. Transition in turbulent flow

As mentioned in Sec. II, many theoretical predictions and experimental observations take the form of power laws $G \sim R^{\alpha}$. As in the analysis of Wendt [13], it is possible to fit our data to two power laws: $\alpha = 1.30$ for $R < 10^4$ and $\alpha = 1.73$ for $R > 10^4$. Although these power laws fit our data well, a closer look at the torque measurements reveals a systematic deviation from power-law behavior.

The high precision of our torque data enables us to determine the local slope $\alpha(R) = \partial(\log_{10}G)/\partial(\log_{10}R)$. The accurate measurement of derivatives is difficult because the process of differentiating naturally increases the noise in any given signal. Several techniques were tried

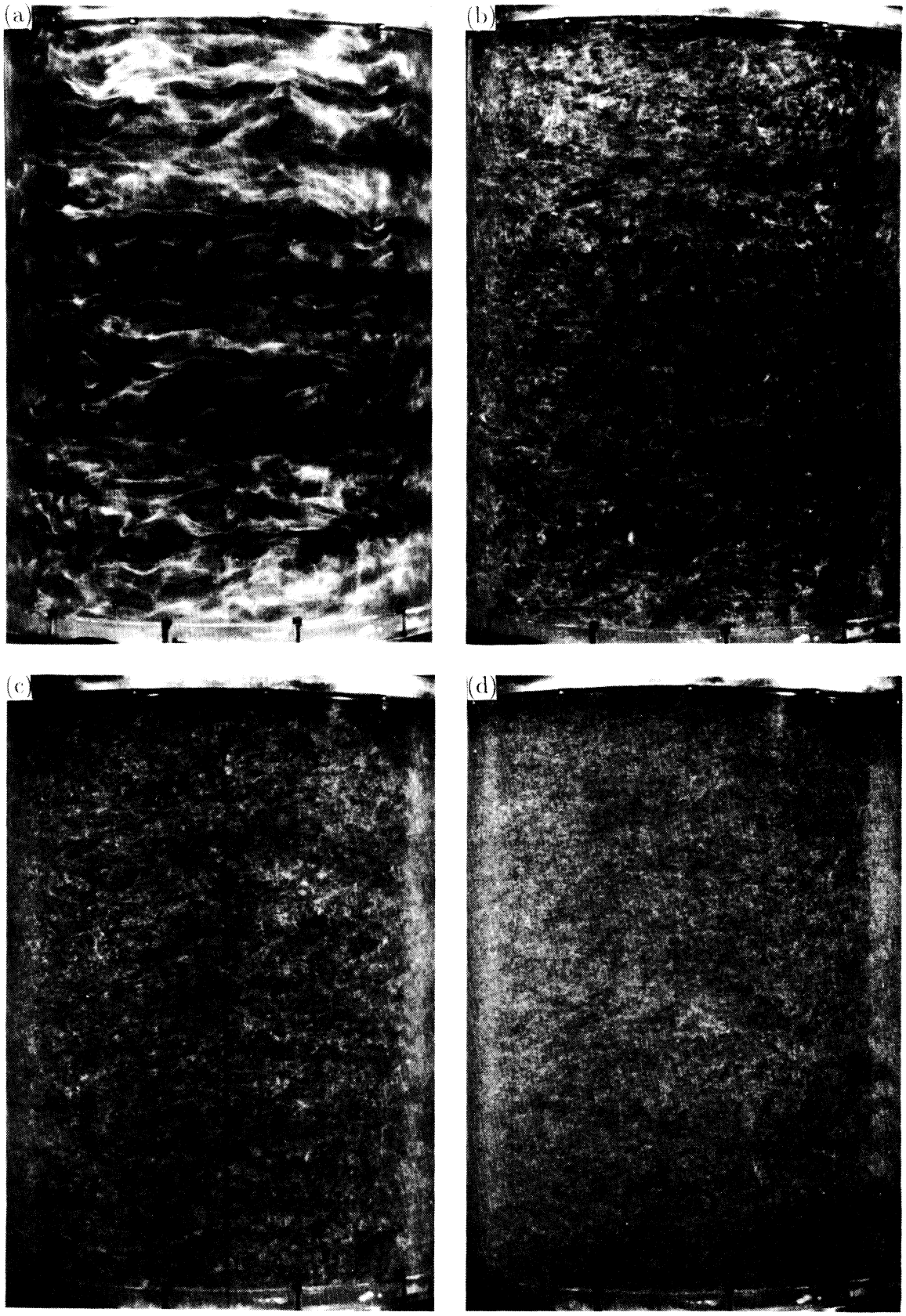

FIG. 5. Photographs of flow states at (a) $R = 6000$, (b) $R = 24\,000$, (c) $R = 48\,000$, and (d) $R = 122\,000$, obtained using Kalliroscope flow visualization. Eight vortices are visible in (a) and (b) and possibly (c), but not in (d).

to determine $\alpha(R)$: forward differencing, center differencing, linear least squares, and polynomial least squares. A practical tradeoff between the locality of the derivative and the accuracy of the slope measurement was obtained using linear least squares to compute the local exponents.

In each case we computed the slopes around points spaced $\Delta\log_{10}R=0.02$ apart, over a window spanning a width $\Delta\log_{10}R<0.1$ (6 or 7 data points). Data from each run were separately analyzed in this way so that uncertainties in viscosity and density do not affect the slope data. The composite slope data were obtained by averaging the slope data from individual runs within bins of width $\Delta\log_{10}R=0.05$. The resultant slope data for eight- and ten-vortex states are presented in Fig. 9.

Surprisingly, there is no range of R in which α is constant. For the eight-vortex data, α increases monotonically from $\alpha=1.23$ to 1.87. Thus there is no Reynolds-number region described by $G\sim R^{\alpha}$.

The slope measurements reveal a sharp transition evidenced by a discontinuity in α at $R_T=1.0\times10^4$ for the ten-vortex data and a sudden change in $\partial\alpha/\partial(\log_{10}R)$ at $R_T=1.3\times10^4$ for the eight-vortex data. The eight-vortex slope data fit the following relation:

$$\alpha=\begin{cases}1.66+0.647\log_{10}(R/R_T)\ , & R<R_T\\ 1.66+0.111\log_{10}(R/R_T)\ , & R>R_T\ .\end{cases}\tag{8}$$

Thus for eight vortices,

$$\log_{10}G=\begin{cases}5.726+0.3235(\log_{10}R)^2\\ \qquad -1.002(\log_{10}R)\ , & R<R_T\\ 1.190+0.0555(\log_{10}R)^2\\ \qquad +1.203(\log_{10}R)\ , & R>R_T\ .\end{cases}\tag{9}$$

The marginal stability exponent $\alpha=\frac{5}{3}$ is not observed over any range of the Reynolds number. This contrasts sharply with Rayleigh-Benard convection, where the marginal stability prediction $\mathrm{Nu}\sim\mathrm{Ra}^{1/3}$ is observed in the range $10^4<\mathrm{Ra}<10^7$. Note that for the eight-vortex state the transition occurs when the local exponent passes through the marginal stability value, and for the ten-vortex state the exponent jumps to approximately the marginal stability value at the transition.

The largest exponent value that we observe, $\alpha=1.87$, is well below the prediction $\alpha=2$ obtained in Eq. (5) from a Kolmogorov-type analysis. This indicates that the torque T has a viscosity dependence (in contrast to the Kolmogorov assumptions), although that dependence is relatively weak, $T\sim\nu^{0.13}$ at the highest Reynolds numbers observed. If Eq. (8) continues to be valid above the Reynolds-number range studied, then the viscosity

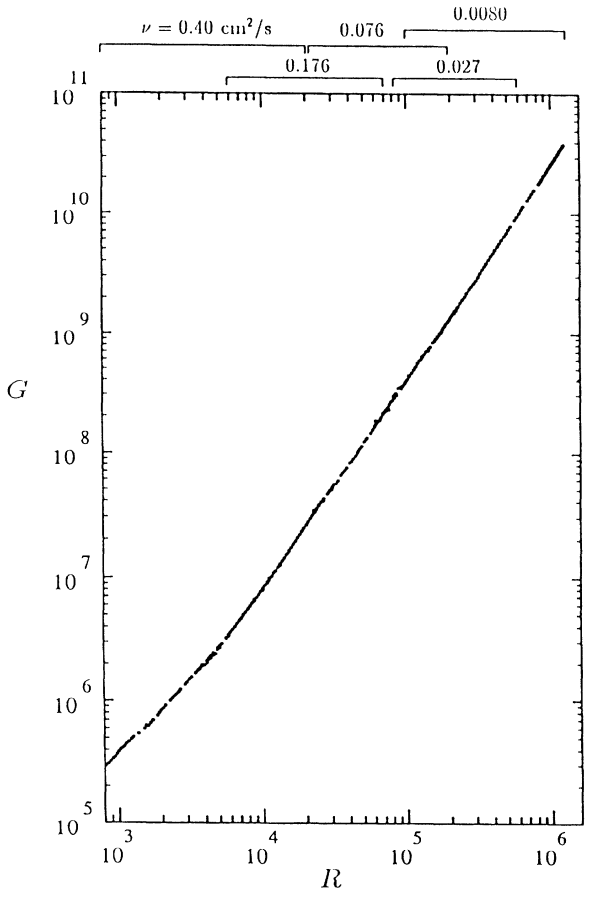

FIG. 6. Experimental measurements for the nondimensional torque for $800<R<1.23\times10^6$, taken for a flow with eight turbulent Taylor vortices for $R<10^5$. The horizontal bars above the graph indicate the Reynolds-number range for each fluid studied.

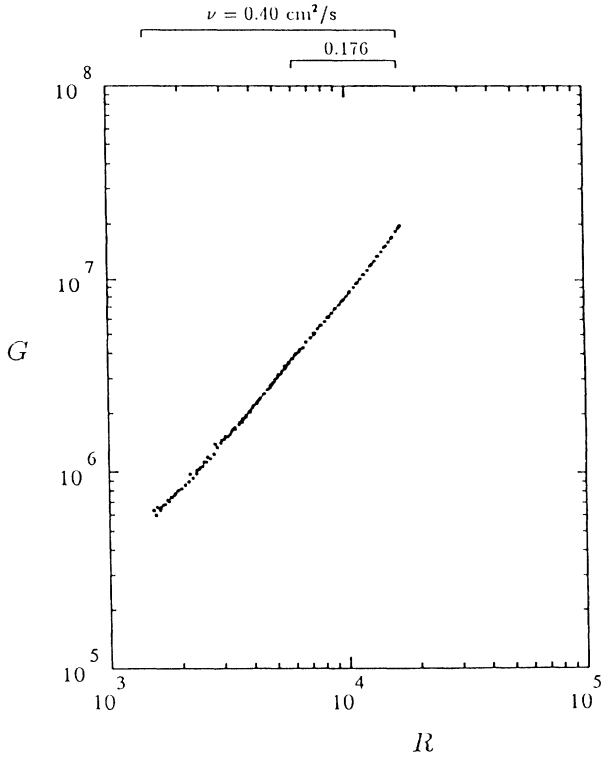

FIG. 7. Experimental measurements for the nondimensional torque for $1.4\times10^3<R<1.75\times10^4$, taken for a flow with ten turbulent Taylor vortices. The horizontal bars above the graph indicate the Reynolds-number range for each fluid studied.

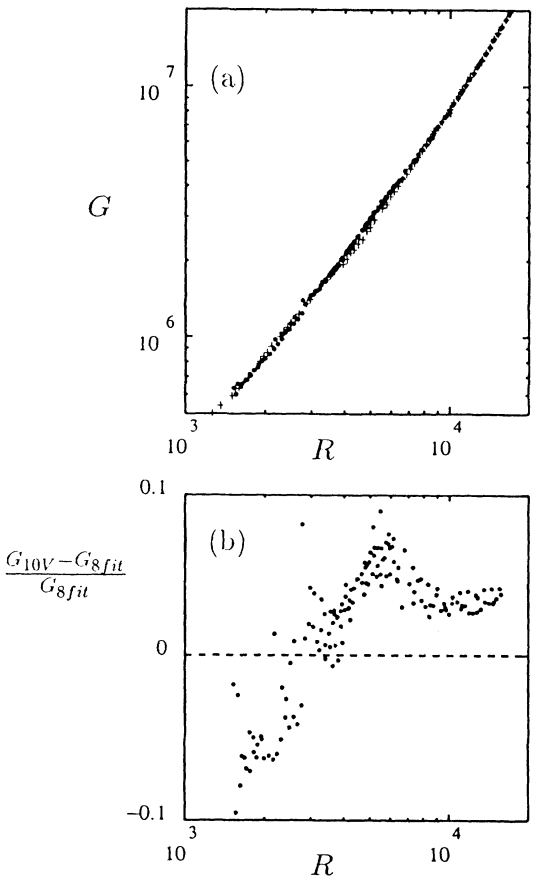

FIG. 8. (a) Comparison of the measured torque G for eight- (+) and ten (·) vortex states as a function of R. (b) Difference between the ten-vortex torque measurements and the torque of the eight-vortex state obtained from Eq. (9).

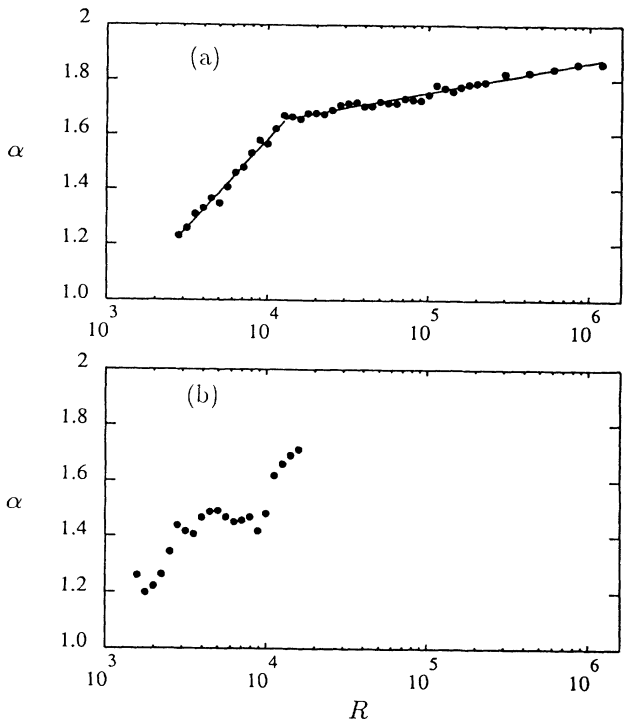

FIG. 9. Local exponent for the torque $\alpha = \partial(\log_{10}G)/\partial(\log_{10}R)$, calculated from torque measurements using least squares over a range $\Delta\log_{10}R = 0.1$: (a) measured for an eight-vortex state (●) and described by Eq. (8) (line); (b) measured for a ten-vortex state (●). At $R = 1.75\times10^4$ the ten-vortex state becomes unstable to the eight-vortex state. For $R > 10^5$, turbulent Taylor vortices are not observed.

dependence would disappear at $R = 1.5\times10^7$, where Eq. (2) yields $\alpha = 2$. Since this is an upper bound for the exponent [25], there must be a departure from Eq. (8) before $R = 1.5\times10^7$.

The deviations from Kolmogorov scaling $\alpha = 2$ may imply a particular form for the velocity fluctuations. We follow the argument backwards, which led to the Kolmogorov $G \sim R^2$ scaling. At a particular Reynolds number, the torque scales as $G = C(\eta)R^\alpha$, where $C(\eta)$ is an unknown function of the radius ratio. The power, given by the torque times the rotation rate, gives the dissipation rate ε:

$$\varepsilon = \nu^{2-\alpha}(\Omega a)^{\alpha+1}(b-a)^{\alpha-3}\left[C(\eta)\frac{(1-\eta)^2}{\pi(1+\eta)\eta}\right]. \quad (10)$$

We then make the reverse substitution from the original argument $\Omega a \to \Delta U$ and $(b-a) \to l$, to find a relation for the velocity differences ΔU:

$$\Delta U \propto \varepsilon^{1/(1+\alpha)}\nu^{(\alpha-2)/(\alpha+1)}l^{(3-\alpha)/(1+\alpha)}, \quad (11)$$

which would lead to a Reynolds-number-dependent velocity structure function. We suggest that this implied deviation from Kolmogorov scaling may hold in this and other wall-bounded shear flows.

C. Comparison with theory and past experiments

Our measurements of the torque show only small deviations from the measurements of Wendt. Figure 10 compares the fits of Wendt [Eq. (2)] with the eight-vortex torque data. Figure 11 shows that although the marginal stability result Eq. (3) does not describe the observed local exponents, it is close in overall magnitude. Figure 11 includes the curves for Couette flow torque and the torque from the Kolmogorov-type calculation [Eq. (5)], which can be considered lower and upper bounds.

VI. BEHAVIOR OF GLOBAL AND LOCAL PROPERTIES

We have shown that the torque measurements do not have a simple Reynolds-number dependence. A complicated dependence on Reynolds number is also observed in other quantities characterizing the flow; however, we find that these quantities are simply related to the global torque. Specifically, we examine the effective axial diffusion coefficients, as measured by Tam and Swinney [33], and the wall shear stress characteristics: time scales, probability distributions, and distributions of the first time derivative.

A. Wall shear stress

We first consider a local quantity, the wall shear stress measured at a single point on the outer cylinder. The

wall shear stress $\tau_w \equiv \rho\nu|\partial u/\partial r|_{r=b}$ is the local quantity corresponding to the torque. The wall shear stress depends on axial position due to the turbulent Taylor vortices, but here we consider τ_w only at a single position, midway between the ends of the annulus. The aximuthal probe size (0.030 cm) is larger than the boundary layer thickness δ (see Table II) for $R > 10^5$; therefore, we only consider wall shear stress data for $R < 10^5$.

The time scales of the fluctuations in τ_w decrease as the Reynolds number increases, as can be seen in the time series in Fig. 12. To quantify this we examine the times between zero crossings for the wall shear stress fluctuations [34,35] $\tau_w' = \tau_w - \overline{\tau_w}$. Figure 13(a) shows histograms of the probability distribution of these zero crossings for two values of the Reynolds number. In the range $10^3 < R < 10^5$ a single distribution function describes all of the zero crossing data when scaled by the mean time $\bar{t}$ between zero crossings, as Figure 13(b) illustrates.

The nondimensional mean time between zero crossings $\bar{t}\nu/(b-a)^2$ characterizes the local time scale in the boundary layer. This can be compared to another estimate of the boundary layer time scale obtained from the global torque measurements. First we estimate the mean boundary layer thickness δ at the outer cylinder, using the definition of the wall shear stress:

$$\overline{\tau_w} = \rho\nu \left| \frac{\overline{\partial u}}{\partial r} \right|_{r=b} \simeq \rho\nu \frac{\gamma\Omega a^2}{b\delta} , \tag{12}$$

where we have assumed a core of constant angular momentum $\mathcal{L} = \gamma\Omega a^2$, and we have used $\gamma = 0.5$ as indicated by measurements of Smith and Townsend [10]. Using the torque measurements to calculate the mean wall shear stress $\overline{\tau_w}$, we solve for the boundary layer thickness:

$$\delta = \frac{\rho\nu\Omega a^2}{2b\overline{\tau_w}} = \frac{\pi abR}{(b-a)G} . \tag{13}$$

The shear velocity u^* is often used as a characteristic velocity within the boundary layer

$$u^* = \left[\frac{\tau_w}{\rho} \right]^{1/2} = \left[\frac{G\nu^2}{2\pi b^2} \right]^{1/2} . \tag{14}$$

We can now define a nondimensional boundary layer time

$$t_{\rm bl} \frac{\nu}{(b-a)^2} \equiv \frac{\delta}{u^*} \frac{\nu}{(b-a)^2} = \frac{R}{G^{3/2}} \frac{\eta(2\pi^3)^{1/2}}{(1-\eta)^3} . \tag{15}$$

In Fig. 14 we compare $t_{\rm bl}$, the boundary layer time from the torque measurements, and $\bar{t}$, the mean time between zero crossings. Both times have the same scaling and show strong curvature in the range $3\times10^3 < R < 2\times10^4$. Thus $\bar{t}$, a local dynamic property of the flow, scales with

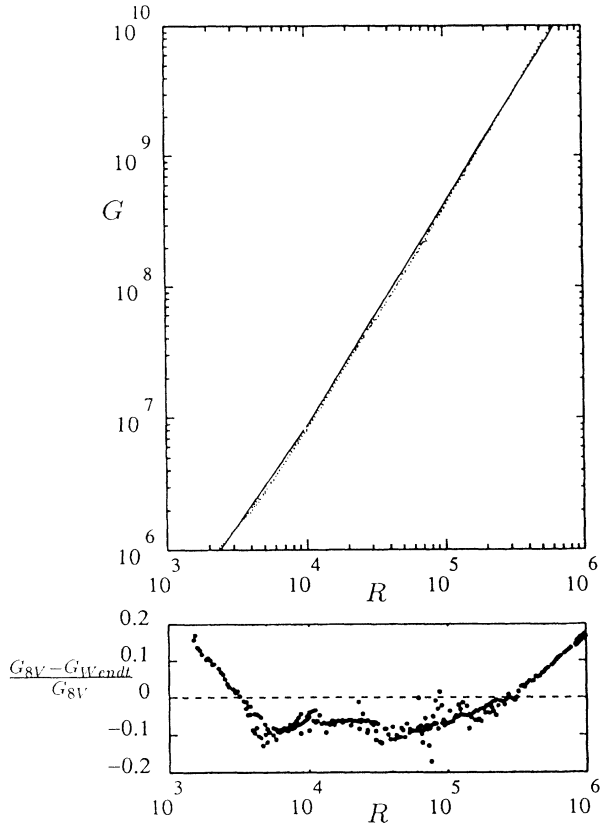

FIG. 10. Measured nondimensional torque for eight vortices (·) compared with fits from Wendt [line, Eq. (2)] [13].

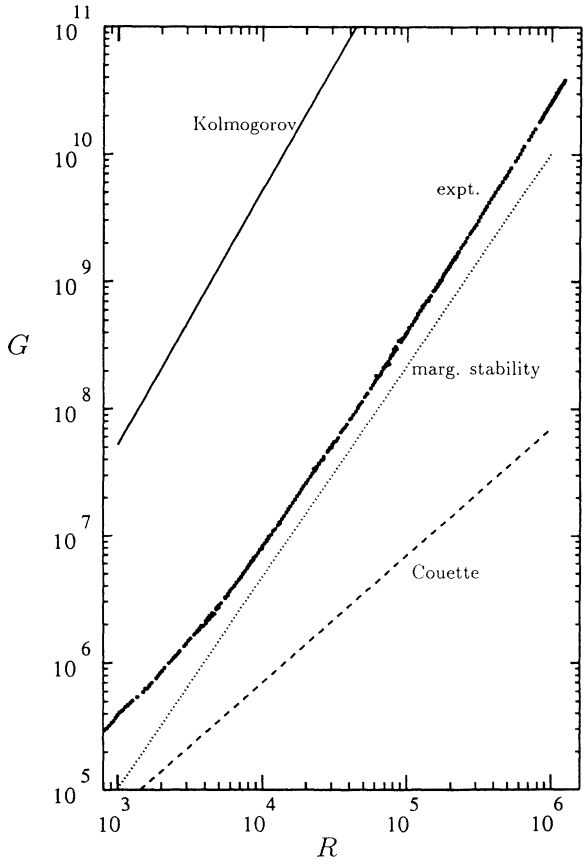

FIG. 11. A comparison of the measured nondimensional torque for eight vortices with the marginal stability prediction [Eq. (3)] [19,20], Couette flow torque [2], $G = 4\pi\eta[(1+\eta)(1-\eta)^2]^{-1}R$, and the Kolmogorov-type prediction [Eq. (5)].

TABLE II. Representative values in an eight-vortex state of the measured nondimensional torque (G), local scaling exponent (α), thickness of the viscous sublayer (at $y^+=5$; see Sec. VII), boundary layer thickness [δ, Eq. (13)], Kolmogorov length [$l_K=(\nu^3/\epsilon)^{1/4}$, where $\epsilon=\nu^2 G\Omega/\pi(b^2-a^2)$], and shear velocity [$u^*$, Eq. (14)].

R	G	α	Thickness of sublayer (cm)	δ (cm)	l_K (cm)	$u^*/\Omega a$
10^3	3.97×10^5	1.27	0.439	0.4612	0.115	0.0693
10^4	8.44×10^6	1.62	0.095 0	0.217	0.030 1	0.0320
10^5	4.21×10^8	1.70	0.013 5	0.043 4	0.006 36	0.0226
10^6	2.68×10^{10}	1.87	0.001 35	0.006 83	0.001 27	0.0180

t_{bl}, a quantity derived solely from a global mean quantity, the torque.

We now consider the distribution functions of the wall shear stress measurements. As shown in Fig. 15(a), the distributions of τ_w exhibit log-normal behavior:

$$P(\tau_w)=(\Lambda e^{\Delta}\sqrt{\pi/\Delta})\exp\{-[\ln(\tau_w/\Lambda)]^2/4\Delta\} . \quad (16)$$

Here Λ is the most probable value of the wall shear stress, and the mean is given by $\overline{\tau_w}=\Lambda e^{3\Delta}$. The standard deviation is given by

$$\sigma_\tau=\overline{\tau_w}(e^{2\Delta}-1)^{1/2} . \quad (17)$$

The value of Δ observed in our experiment is 0.22 ± 0.03 over the range of Reynolds numbers studied with the hot film probe. As can be seen in Fig. 15(a), values of τ_w that are several times the mean value can be observed in the distribution. The observed standard deviation of the wall shear stress σ_τ scales simply with the mean of the wall shear stress (and therefore with the torque), as is illustrated in Fig. 16(a) and is suggested by Eq. (17). Here we again find that a *local* property scales simply with the global torque measurements.

This behavior is further seen in the Reynolds-number dependence of the first time derivative of the wall shear stress data. The time derivatives were estimated by a sliding least-squares procedure applied over a time $\Delta t=2.7\times10^{-7}(b-a)^2/\nu$. A typical probability distribution of $\partial\tau_w/\partial t$ is shown in Fig. 15(b). These distribu-

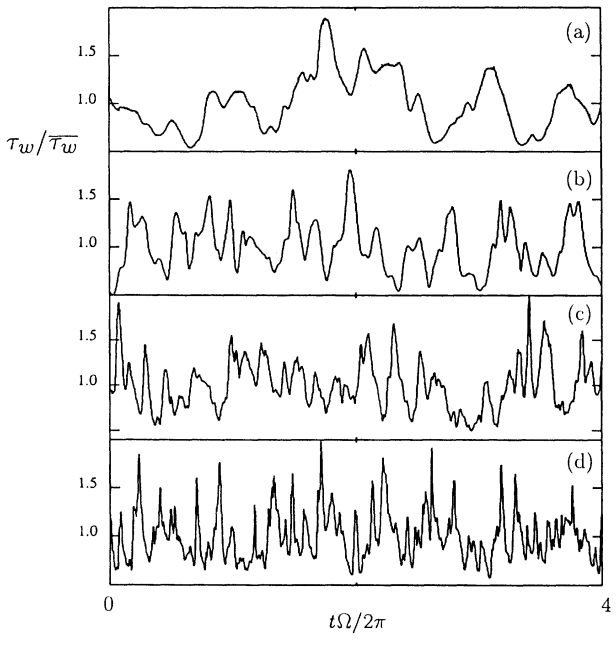

FIG. 12. Time series of the wall shear stress from a hot film probe for (a) $R=6800$, (b) $R=16\,000$, (c) $R=44\,000$, and (d) $R=120\,000$. The sequence illustrates the decrease in time scales with increasing Reynolds number. Each time series is over four inner cylinder rotation periods.

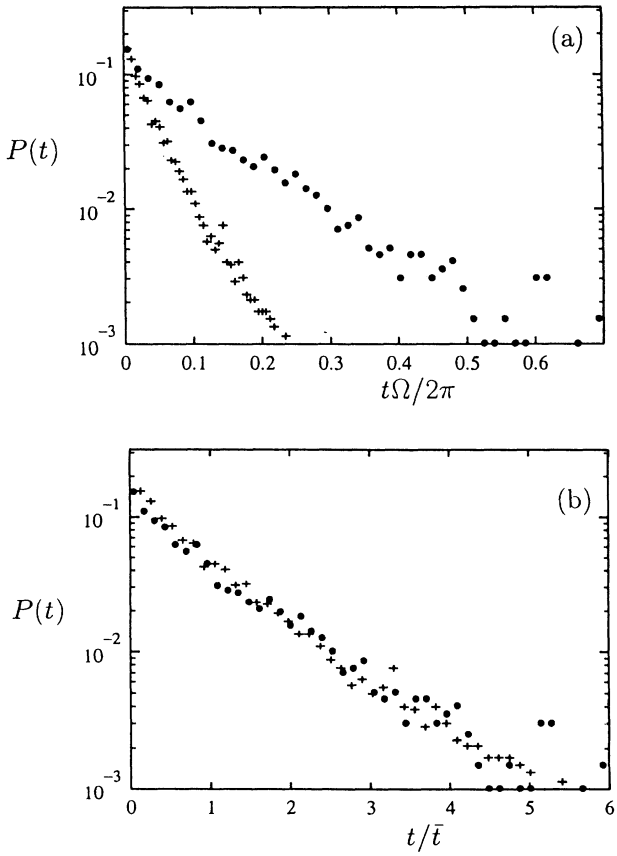

FIG. 13. Probability distribution for the time between zero crossings of the wall shear stress fluctuations $\tau_w'=\tau_w-\overline{\tau_w}$, for $R=6.10\times10^4$ (●) and for $R=1.22\times10^5$ (+). (a) The unnormalized times. (b) The times between zero crossings t normalized by the mean $\bar{t}$.

tions are skewed with asymmetric exponential tails similar to the velocity derivative distribution functions observed in homogeneous turbulent flow [36] (but with skewness of opposite sign); the asymmetry is clear in Fig. 15(c), which is on an expanded scale. Figure 16(b) compares the standard deviation of the time derivative distributions $\sigma_{\partial\tau_w/\partial t}$ as a function of Reynolds number with the ratio $\sigma_\tau/t_{\rm bl}$; the graph demonstrates that the distributions of the time derivatives scale with the wall shear stress and time scales already observed in the system.

B. Turbulent diffusion

The turbulent transport of passive scalars in the axial direction of a Couette-Taylor system was investigated experimentally by Tam and Swinney [33]. They injected dye into the fluid and measured the time dependence of its concentration at different axial positions. Those measurements indicated that the dye transport could be well modeled by a diffusive process. Although the effective diffusion coefficient $D_{\rm eff}$ was found to scale roughly as $D_{\rm eff}\sim R^\beta$, the scaling exponent β increased as a function of the Reynolds number, as in our torque measurements. We can relate these transport measurements to the torque by making use of the Reynolds analogy [37], which asserts that the effective momentum diffusion coefficient ν_t (the turbulent viscosity) is proportional to the turbulent diffusivity of a passive scalar: $\nu_t = cD_{\rm eff}$ (where c is an unknown prefactor). This untested hypothesis is widely used in the analysis of turbulence [37]

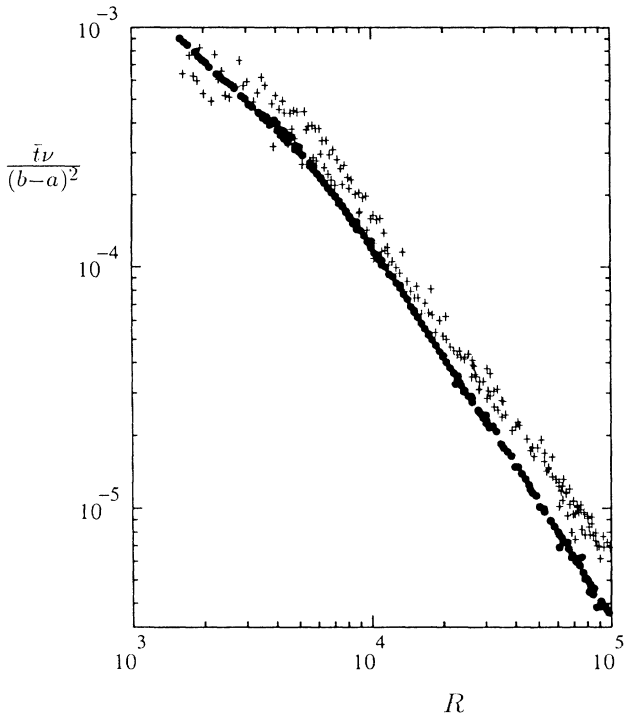

FIG. 14. Time scales from the mean time $\bar{t}$ between zero crossings (+) for the wall shear stress fluctuations $\tau_w' = \tau_w - \overline{\tau_w}$, and the boundary layer time $t_{\rm bl} = \delta/u^*$ obtained from the torque measurements (●) [see Eq. (15)]. Both times have been nondimensionalized using the viscous time $(b-a)^2/\nu$.

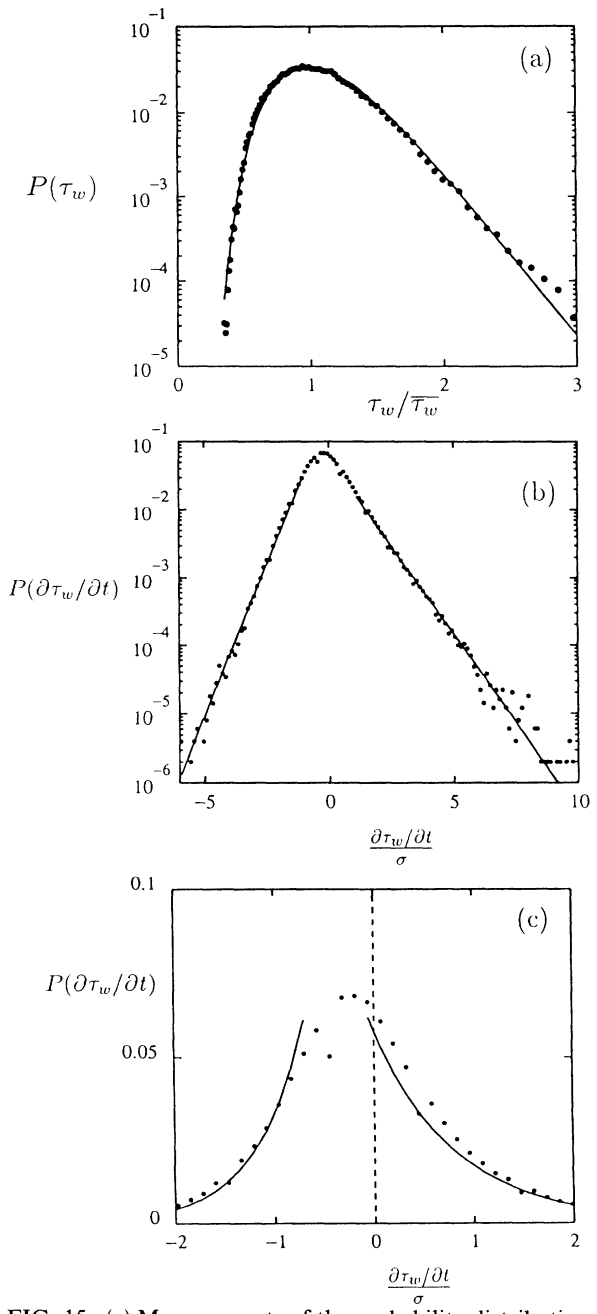

FIG. 15. (a) Measurements of the probability distribution for the wall shear stress (●) at $R = 1.22\times10^5$, compared with a fit to a log-normal distribution (line), $\log_{10}P(\tau_w) = -13.6(\log_{10}\tau_w)^2 - 0.175\log_{10}\tau_w - 1.46$. (b) Measurements of the probability distribution for the time derivative of the wall shear stress $\partial\tau_w/\partial t$ at $R = 1.22\times10^5$, as calculated locally using a least-squares procedure over the time $\Delta t = 2.7\times10^{-7}(b-a)^2/\nu$. The lines are exponential distributions $P = 0.0574e^{-x/0.839}$ for $x>0$ and $P = 0.258e^{x/0.488}$ for $x<0$, where $x = (\partial\tau_w/\partial t)/\sigma$ and σ is the standard deviation of $\partial\tau_w/\partial t$. (c) The central part of the probability distribution function shown in (b) with the probability on a linear rather than logarithmic scale; the two curves show the result from the exponential fits to the tails of the distribution function. The distributions were formed from a 5×10^5 point time series for the wall shear stress, which was sampled at 2048 points per revolution of the inner cylinder.

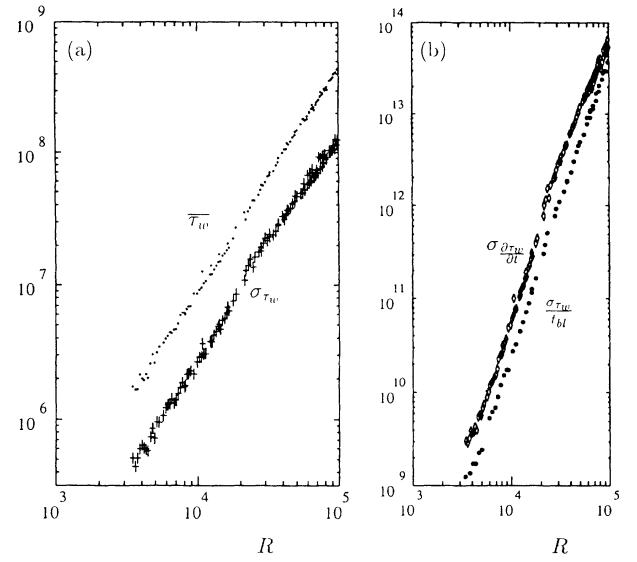

FIG. 16. (a) A comparison of the mean wall shear stress $\overline{\tau_w}$ with the standard deviation of the wall shear stress σ_{τ_w}. Both quantities have been made nondimensional by multiplying by $2\pi b^2/\rho\nu^2$. (b) A comparison of the standard deviation of the first time derivative $\sigma_{\partial\tau_w/\partial t}$ with $\sigma_{\tau_w}/t_{\rm bl}$, the ratio of the standard deviation of the wall shear stress and the boundary layer time $t_{\rm bl}$. Both quantities have been made nondimensional by multiplying by $2\pi b^2(b-a)^2/(\rho\nu^3)$.

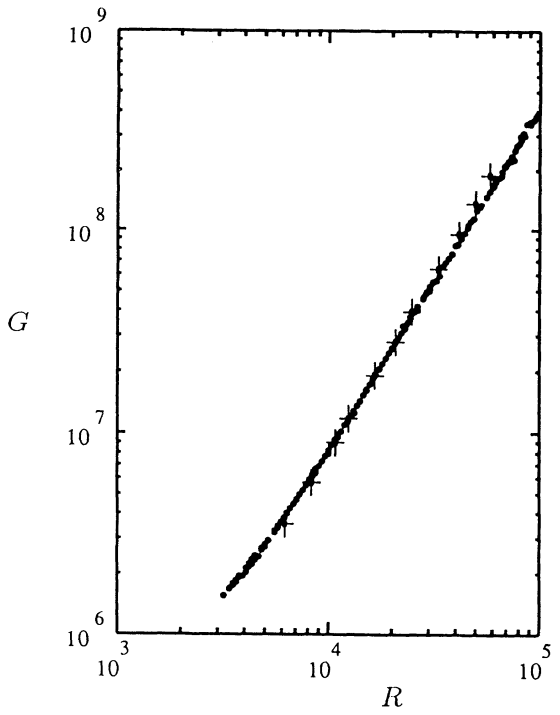

FIG. 17. A comparison of the torque computed from the axial diffusion measurements (+) [see Eq. (18)] with the measured torque (●).

and is crucial for understanding the interior structure of stars [38]. As we will now show, our measurements provide direct support for the Reynolds analogy.

To calculate the torque we estimate the flux J of angular momentum $\mathcal{L}$ across the gap:

$$J=\nu_t\left[\frac{\mathcal{L}(r=a)-\mathcal{L}(r=b)}{b-a}\right]=cD_{\rm eff}\left[\frac{\rho a^2\Omega}{b-a}\right]. \tag{18}$$

The torque is given by the angular momentum flux times the area A of the inner cylinder:

$$G=\frac{JA}{\rho\nu^2L}=\frac{2\pi\eta^2cD_{\rm eff}R}{(1-\eta)^2\nu}, \tag{19}$$

where we have divided by $\rho\nu^2L$ to nondimensionalize the torque. In Fig. 17 we compare the measured torque [39] with estimates of the torque using Eq. (19) (with $c=0.176$). The good agreement supports the assumption that the diffusion of momentum is proportional to the diffusion of a passive scalar in turbulent flow. The agreement is within the experimental uncertainty, although the dye transport data do not have sufficient precision to reveal the transition at R_T. The nonunity value of the constant c may indicate anisotropy between radial and axial transport.

In conclusion, we find that local quantities such as the turbulent axial diffusivity, the local characteristic times scales, the distributions of the wall shear stress, and the distributions of its first time derivative are simple scaling functions of a global quantity, the torque G, and the Reynolds number R.

VII. SHEAR FLOW TURBULENCE

We now will show that above R_T the flow behavior is similar to that of wall-bounded shear flows characterized by a turbulent boundary layer. In Sec. VI we observed that a local quantity, the mean zero crossing time $\bar{t}$, characterizes the time scales observed in the boundary layer as the Reynolds number of the system is varied. Measurements of $\bar{t}$ were also performed by Shah and Antonia [35] for flow in a duct at large Reynolds numbers. In Fig. 18 we directly compare the values of $\bar{t}$ for the two different flows. The excellent quantitative agreement above R_T of the Couette-Taylor and the duct flow time scales suggests that above R_T (1.3×10^4), the flow in our system may be similar to turbulent wall-bounded shear flows in open systems.

Turbulent boundary layers have been extensively studied in pipe flow, plane channel flow, and flow over a flat plate. In these cases the mean velocity profile $u(y)$ approaches a universal form when scaled by the shear velocity $u^*\equiv\sqrt{\tau_w/\rho}$ and the distance from the wall y is scaled using $y^+=yu^*/\nu$ ($y=0$ at the wall). A typical boundary layer contains a viscous sublayer for $y^+<5$ with the velocity profile $u^+=u/u^*=y^+$, connected to a logarithmic layer that extends over a large range of y^+ at large Reynolds numbers [40]. In this logarithmic boundary layer the mean velocity profile takes on the simple form $u^+=A\log_{10}y^++B$, where $A=5.75=(\ln10)/\kappa$, $B=5.5$, and κ is the von Kármán constant [41–43].

This velocity profile can be derived by assuming that along an infinite plate, the mean shear stress σ in a turbulent flow is constant, independent of y. Thus the aver-

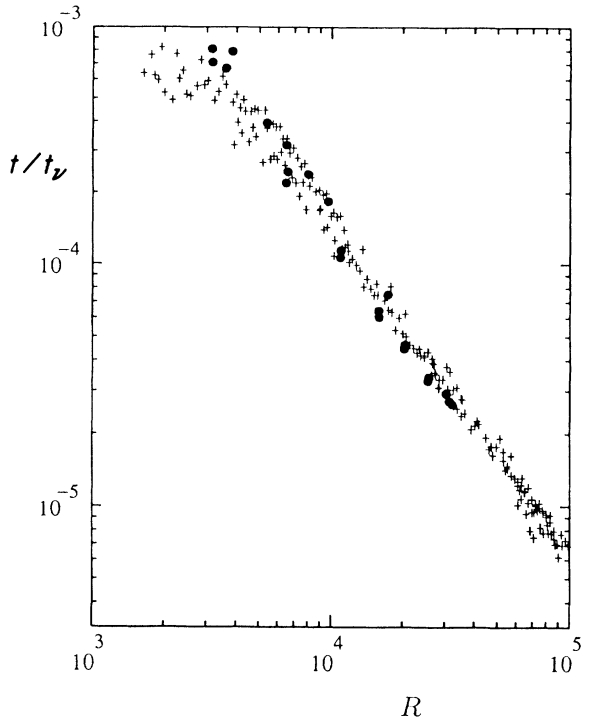

FIG. 18. Time scales of the mean time between zero crossings for the wall shear stress fluctuations τ'_w ($\tau'_w=\tau_w-\overline{\tau_w}$), measured in the present experiment (+) and compared with measurements by Shah and Antonia for duct flow [35] (●). Both times have been nondimensionalized using the viscous times t_ν: $(b-a)^2/\nu$ for Couette-Taylor and d^2/ν for a duct of width d. The Reynolds number for duct flow is $R=u_0 d/\nu$ for centerline velocity u_0.

age streamwise *linear* momentum transmitted in the y direction by each fluid layer is constant [44]. To derive an analogous expression for the mean velocity profile in our flow, we shall use the Prandtl [45] expression for the form of $\sigma(y)$ in turbulent flow:

$$\sigma(y)=\rho\kappa^2 y^2\left[\frac{du}{dy}\right]^2 . \tag{20}$$

In cylindrical coordinates Eq. (20) becomes

$$\sigma(r)=\rho\kappa^2(b-r)^2\left[\frac{du}{dr}\right]^2 , \tag{21}$$

where we consider the distance $b-r$ from the outer cylinder wall.

In our system the conserved quantity in the flow is the flux of *angular* momentum (proportional to the torque) and not the flux of linear momentum transferred by each fluid layer. Using this we obtain the following expression for σ as a function of the radius r:

$$\sigma(r)=\frac{T}{rA}=\frac{\rho\nu^2 G}{2\pi r^2} , \tag{22}$$

where $T=\rho\nu^2 LG$ is the torque and A the area of a cylindrical fluid element at radius r. Equating the two expressions for $\sigma(r)$ we find

$$\frac{du}{dr}=\frac{\nu}{\kappa}\left[\frac{G}{2\pi}\right]^{1/2}\frac{1}{r(b-r)} . \tag{23}$$

Integration of Eq. (23) yields the azimuthal velocity profile $u_{\rm out}(r)$ near the outer wall:

$$u_{\rm out}(r)=\frac{\nu}{\kappa b}\left[\frac{G}{2\pi}\right]^{1/2}\left[\ln\left[\frac{b-r}{r}\right]+C\right] . \tag{24}$$

The constant of integration C in Eq. (24) is determined by matching $u_{\rm out}(r)$ with the viscous sublayer at $y^+\equiv y_0^+=5$ [46]; $u_{\rm out}(y^+=y_0^+)=y_0^+ u^*$. Here $u^*=(\nu/b)(G/2\pi)^{1/2}$ is the shear velocity at the outer wall. We then obtain

$$u_{\rm out}(r)=\frac{u^*}{\kappa}\left[\ln\left\{\left[\frac{b-r}{r}\right]\left[\frac{u^* b}{\nu y_0^+}-1\right]\right\}+\kappa y_0^+\right] . \tag{25}$$

Note that the expression for $u_{\rm out}$ becomes the more familiar expression for the velocity profile of the logarithmic layer in the limit where the radius of the outer cylinder becomes infinite. [This can be seen by writing Eq. (25) in terms of the distance from the wall $y=(b-r)$.]. In a similar fashion the expression for the azimuthal velocity profile $u_{\rm in}(r)$ near the inner cylinder becomes

$$u_{\rm in}(r)=\Omega a-\frac{u^*}{\kappa\eta}\left[\ln\left\{\left[\frac{r-a}{r}\right]\left[\frac{u^* b}{\nu y_0^+}+1\right]\right\}+\kappa y_0^+\right] , \tag{26}$$

where we used the fact that shear velocity at the inner wall must satisfy $u^*=u^*_{\rm in}\eta$ for the torques to be equal at the inner and outer cylinders.

We now assume that the mean velocity profile outside of the viscous sublayers is composed of the two logarithmic boundary layers given by Eqs. (25) and (26) that match at midgap. We can use this profile to calculate the dependence of the torque on the Reynolds number. Thus equating $u_{\rm in}$ and $u_{\rm out}$ at $r=(b+a)/2$ we find (when $G\gg 1$)

$$\frac{R}{\sqrt{G}}=N\log_{10}\sqrt{G}+M , \tag{27}$$

with $N=[(1-\eta^2)\ln 10]/\eta\kappa\sqrt{2\pi}=1.50$ and

$$M=N\left[\ln\left\{\left[\frac{1-\eta}{1+\eta}\right]\frac{1}{y_0^+\sqrt{2\pi}}\right\}+\kappa y_0^+\right]=-1.56 .$$

Defining the skin friction coefficient [47] as $c_f=G/R^2=2\pi b^2\tau_w/\rho\nu^2R^2$, Eq. (27) becomes

$$\frac{1}{\sqrt{c_f}}=N\log_{10}R\sqrt{c_f}+M . \tag{28}$$

Equation (28), which is analogous to the Prandtl–von Kármán skin friction law [40,42], predicts a linear relationship between $1/\sqrt{c_f}$ and $\log_{10}R\sqrt{c_f}$. We test this linear relationship in Fig. 19 for $R>R_T$ and find reasonable agreement with both the predicted form and coefficients. By linear regression the data yield $N=1.52$

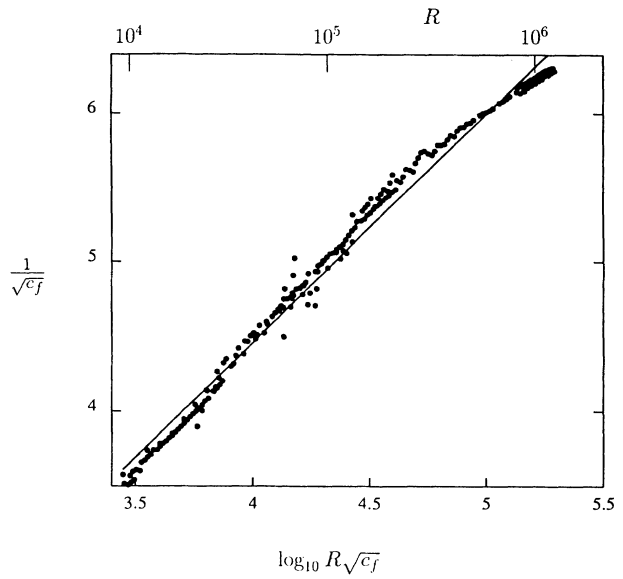

FIG. 19. A comparison of a Prandtl–von Kármán-type skin friction law (solid line) with the experimental torque data (●) [Eq. (28)].

and $M=-1.63$. This value of N yields a von Kármán constant $\kappa=[(1-\eta^2)\ln 10]/(\sqrt{2\pi}N\eta)=0.40$, which is in excellent agreement with the value of $\kappa=0.41$ observed in pipe flow; the value of M (-1.63) obtained from the fit is within 5% of the value given by Eq. (28) (-1.56). Figure 20 compares the observed torque with that from the Prandtl–von Kármán form with the empirical coefficients. The local exponent for the model can be calculated from Eq. (28):

$$\alpha=\left[\frac{1}{2}+\frac{\log_{10}e}{\left[\log_{10}G+\frac{2M}{N}\right]}\right]^{-1}. \tag{29}$$

This local exponent displays the slow variation in local exponent α observed in the experiment for $R>R_T$, as Fig. 21 illustrates.

Although this model does not explicitly use a core of constant angular momentum density, the model gives a core region with angular momentum density $\mathcal{L}/\Omega a^2=0.5$ (within 2%), as shown in Fig. 22. Thus the angular momentum density for this model shows the same qualitative form as in the measurements of Smith and Townsend [10]; however, the measured boundary layer thickness is much smaller than that given by the Prandtl–von Kármán model.

The agreement between the observed torque and the Prandtl–von Kármán model suggests a direct comparison between the skin friction coefficient that we observed, and those for pipe flow and flow over a flat plate. The skin friction coefficient (the dimensionless drag force) is defined as $c_f=8\tau_w/\rho\bar{u}^2$ for pipe flow, where $\bar{u}$ is the mean velocity, and $c_f=2\tau_w/\rho u_\infty^2$ for flow over a flat plate, where u_∞ is the velocity far from the plate [42].

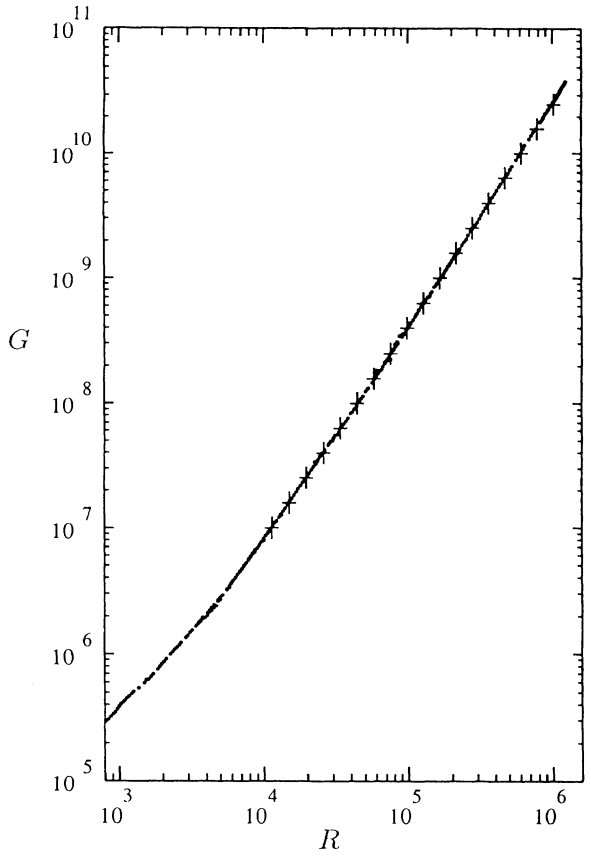

FIG. 20. The measured nondimensional torque for eight vortices (·) compared with the Prandtl–von Kármán model (+) [Eq. (28)] with $N=1.52$ and $M=-1.63$.

The Reynolds numbers used for comparison are $R=\bar{u}d/\nu$ for pipe flow (where d is the diameter of the pipe) and $R=u_\infty x/\nu$ for flow over a flat plate (where x is the distance from the leading edge of the plate) [42]. Since the Reynolds numbers are defined in different ways, we scale them using a transition Reynolds number R_T. In our system the transition occurs in the presence of centrifugally driven disturbances. For the other wall-bounded shear flows, we choose the minimum transition

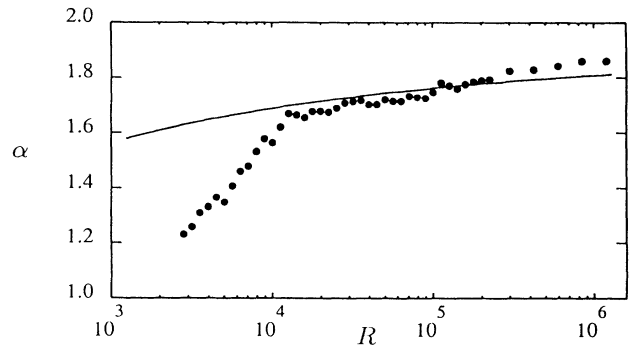

FIG. 21. The measured local exponent α for the eight-vortex state (●) compared with the local slope from the Prandtl–von Kármán model [line, Eq. (29)].

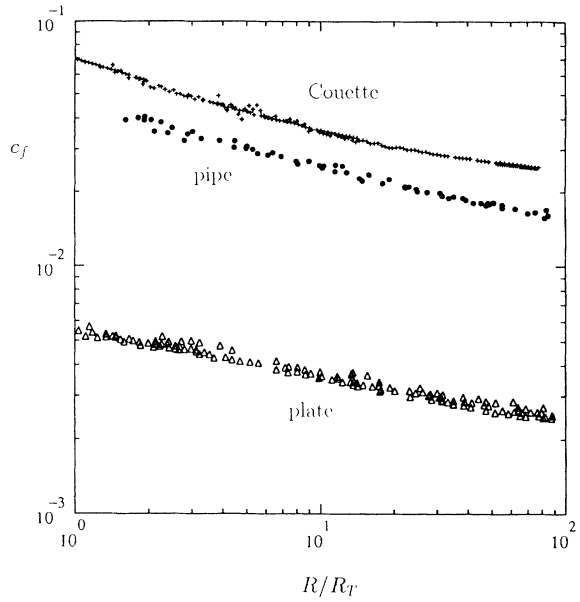

FIG. 22. The angular momentum density for the two logarithmic layer model $\mathcal{L}=\overline{ru_\theta(r)}$ normalized by the specific angular momentum of the inner cylinder Ωa^2 for $R=5.03\times10^4$ (solid line), $R=10^6$ (dotted line), and as measured by Smith and Townsend (+) at $R=5.03\times10^4$ [10].

Reynolds number for the transition to turbulent shear flow in the presence of disturbances. The transition Reynolds numbers used are $R_T=1.3\times10^4$ for the Couette-Taylor system, $R_T=2.3\times10^3$ for pipe flow [42], and $R_T=3.2\times10^5$ for flow over a flat plate [42].

As can be seen in Fig. 23, the skin friction coefficients

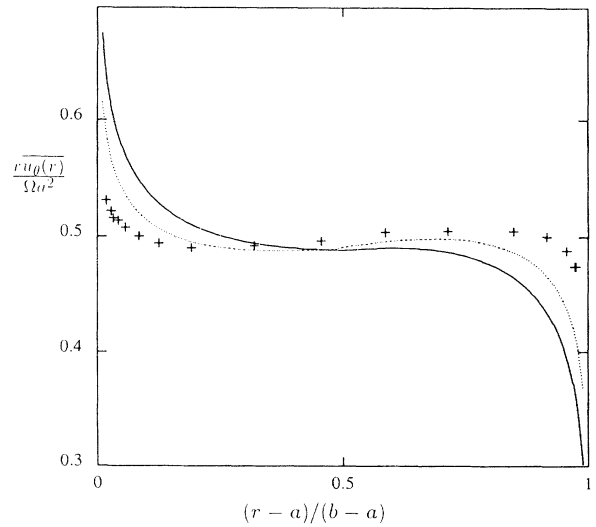

FIG. 23. Skin friction coefficients for turbulent flows for the Couette-Taylor system, a pipe, and a flat plate (with zero pressure gradient), as a function of R/R_T, where R_T is taken to be the transition Reynolds number in the presence of background disturbances. ($R_T=1.3\times10^4$ for Taylor vortex flow, 2.3×10^3 for pipe flow, and 3.2×10^5 for a flat plate.)

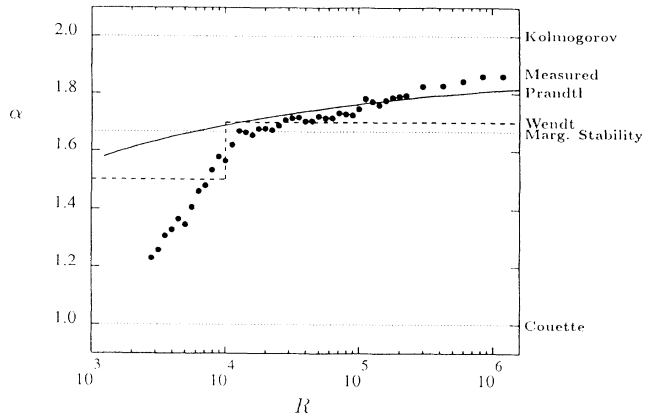

FIG. 24. A summary of theory and experiments for the local exponent for the torque, $\alpha=\partial(\log_{10}G)/\partial(\log_{10}R)$, including the Kolmogorov-type estimate (dotted line, $\alpha=2$), the measured exponent for an eight-vortex state (●), the local exponent from the Prandtl–von Kármán-type estimate [solid line, Eq. (29)], the fit from the experiments of Wendt [dashed line, Eq. (2)], the marginal stability estimate of Marcus (dotted line, $\alpha=\frac{5}{3}$), and the exponent for Couette flow torque (dotted line, $\alpha=1$).

for these three systems exhibit the same qualitative behavior with Reynolds number, decreasing monotonically with upward concavity. This and the agreement with the boundary layer time scales from duct flow suggest that there may be a single fluid dynamical description for all turbulent wall-bounded shear flows. *A priori* one might have expected major differences between the closed Couette-Taylor system, where the transition is nonhysteretic, and open flows such as pipe flow, duct flow, and flow over a flat plate, where the transition shows large hysteresis. The similarity is also surprising considering the differences in downstream and radial pressure gradients and differences in wall curvature.

VIII. CONCLUSIONS

We performed high-precision torque measurements over a large range of Reynolds number. No simple power-law scaling for the torque $G\sim R^\alpha$ describes the observed results over any range of Reynolds number, as is shown by the results for $\alpha(R)$ summarized in Fig. 24. The deviations from a Kolmogorov-type calculation (predicting $\alpha=2$) lead us to suggest that the typical velocity fluctuations ΔU follow a scaling $\Delta U\sim l^{(3-\alpha)/(1+\alpha)}$ for separations l.

In addition, we have found that above a nonhysteretic transition at $R_T=1.3\times10^4$ this closed system behaves like open wall-bounded shear flows (pipe flow, duct flow, and flow over a flat plate) at high Reynolds numbers, including conformity to a Prandtl–von Kármán-type skin friction law.

Although the torque was observed to be a nontrivial function of Reynolds number, other measured flow properties (axial diffusivity, local time scales, and distributions of local quantities) are simple scaling functions of the torque and Reynolds number.

ACKNOWLEDGMENTS

We would like to acknowledge helpful discussions with R. P. Behringer, M. E. Crawford, C. Doering, P. S. Marcus, R. L. Panton, E. D. Siggia, B. Shraiman, E. A. Spiegel, and J. Weldon. This work is supported by ONR Grant No. N000014-89-J-1495. Jay Fineberg was supported in part by IBM.

*Present address: Dunham Laboratory, Yale University, New Haven, CT 06520-1968.

†Electronic address: swinney@chaos.utexas.edu

[1] D. P. Lathrop, J. Fineberg, and H. L. Swinney, Phys. Rev. Lett. **68**, 1515 (1992).

[2] R. C. Di Prima and H. L. Swinney, in *Hydrodynamic Instabilities and the Transition to Turbulence,* edited by H. L. Swinney and J. P. Gollub (Springer-Verlag, Berlin, 1985), p. 139.

[3] K. Kataoka, *Taylor Vortices and Instabilities in Circular Couette Flows,* in *Encyclopedia of Fluid Mechanics,* edited by N. P. Cheremisinoff (Gulf, Houston, 1986), Vol. 1, p. 236.

[4] P. R. Fenstermacher, H. L. Swinney, and J. P. Gollub, J. Fluid Mech. **94**, 103 (1979).

[5] A. Brandstater and H. L. Swinney, Phys. Rev. A **35**, 2207 (1987).

[6] J. P. Gollub and H. L. Swinney, Phys. Rev. Lett. **35**, 927 (1975).

[7] G. I. Taylor, Philos. Trans. R. Soc. London A **223**, 289 (1923).

[8] D. Coles, J. Fluid Mech. **21**, 385 (1965).

[9] See, for example, the torque measurements of R. J. Donnelly and N. J. Simon, J. Fluid Mech. **7**, 401 (1960) and K. Nakabayashi, Y. Yamada, and T. Kishimoto, *ibid.* **119**, 409 (1982).

[10] G. P. Smith and A. A. Townsend, J. Fluid Mech. **123**, 187 (1982).

[11] A. A. Townsend, J. Fluid Mech. **144**, 329 (1984).

[12] K. Kataoka, Y. Bitou, K. Hashioka, T. Komai, and H. Doi, in *Heat and Mass Transfer in Rotating Machinery,* edited by D. E. Metzger and N. H. Afgan (Hemisphere, Washington, D.C., 1984).

[13] F. Wendt, Ingenieur-Archiv. **4**, 577 (1933).

[14] G. I. Taylor, Proc. R. Soc. London, Ser. A **157**, 546 (1936).

[15] P. Tong, W. I. Goldburg, J. S. Huang, and T. A. Witten, Phys. Rev. Lett. **65**, 2780 (1990).

[16] B. Castaing, G. Gunaratne, F. Heslot, L. Kadanoff, A. Libchaber, S. Thomae, X.-Z. Wu, S. Zaleski, and G. Zanetti, J. Fluid Mech. **204**, 1 (1989).

[17] F. Heslot, B. Castaing, and A. Libchaber, Phys. Rev. A **36**, 5870 (1987), and references therein.

[18] W. V. R. Malkus and G. Veronis, J. Fluid Mech. **4**, 225 (1958).

[19] P. S. Marcus, J. Fluid Mech. **146**, 65 (1984).

[20] G. P. King, Y. Li, W. Lee, H. L. Swinney, and P. S. Marcus, J. Fluid Mech. **141**, 365 (1984).

[21] D. P. Lathrop, Ph. D. dissertation, The University of Texas at Austin, 1992.

[22] A. Barcilon and J. Brindley, J. Fluid Mech. **143**, 429 (1984).

[23] A. N. Kolmogorov, C. R. Dokl. Acad. Sci. URSS **30**, 301 (1941).

[24] E. C. Nickerson, J. Fluid Mech. **38**, 807 (1969).

[25] C. R. Doering and P. Constantin, Phys. Rev. Lett. **69**, 1648 (1992).

[26] The outer cylinder was supplied by Reynolds Polymer Technologies Inc., 311 E. Alton, Santa Ana, CA 92707.

[27] The inner radius of the central section of the outer cylinder, where the torque measurements were made, was measured at six equally spaced angles at three axial positions (midheight and ± 18 cm from midheight). The radius was found to have root-mean-square variation less than 30 μm in measurements separated by $2\frac{1}{2}$ years, but during that time the radius increased by 200 μm, presumably due to fluid absorption.

[28] The maximum Reynolds number is set by the available motor power and is attained at a rotation rate of $\Omega/2\pi = 16.5$ Hz in water.

[29] R. J. Goldstein, *Fluid Mechanics Measurements* (Hemisphere, Washington, D. C., 1983).

[30] P. Matisse and M. Gorman, Phys. Fluids **27**, 759 (1984).

[31] O. Savas, J. Fluid Mech. **152**, 235 (1985).

[32] This flow visualization technique is not sufficient to determine quantitatively the point at which the Taylor vortices disappear or the mechanism by which this occurs.

[33] W. Y. Tam and H. L. Swinney, Phys. Rev. A **36**, 1374 (1987).

[34] K. R. Sreenivasan and R. A. Antonia, J. Appl. Mech. **44**, 389 (1977); K. R. Sreenivasan, A. Prabhu, and R. Narasimha, J. Fluid Mech. **137**, 251 (1983).

[35] D. A. Shah and R. A. Antonia, AIAA J. **25**, 22 (1987).

[36] C. A. Van Atta and W. Y. Chen, J. Fluid Mech. **44**, 145 (1970).

[37] W. M. Kays and M. E. Crawford, *Convective Heat and Mass Transfer* (McGraw-Hill, New York, 1980), p. 207.

[38] B. Chaboyer and J. P. Zahn, Astron. Astrophys. **253**, 173 (1992).

[39] The values of D_{eff} used for the comparison [33] were for the same axial wave number as the torque measurements.

[40] R. L. Panton, *Incompressible Flow* (Wiley, New York, 1984), p. 209.

[41] The coefficients $A = 5.75$ and $B = 5.5$ are taken from measurements from pipe flow [43], the coefficients for flow over a flat plate with zero pressure gradient have been measured to be 5.85 and 5.56 [42].

[42] H. Schlichting, *Boundary-Layer Theory,* 7th ed. (McGraw-Hill, New York, 1979), p. 598, p. 639, and p. 641.

[43] J. Nikuradse, Forsch. Arbeit Ingenieur-Westfalen **356**, 36 (1932).

[44] L. D. Landau and E. M. Lifshitz, *Fluid Mechanics,* 2nd ed. (Pergamon, Oxford, 1987), p. 158.

[45] L. Prandtl, Angew. Math. Mech. **5**, 136 (1925).

[46] The results derived in Eqs. (27) and (28) are not affected by the exact value of y_0^+ chosen for the matching of the logarithmic velocity profile to that of the viscous sublayer. For $1 < y_0^+ < 5$ the value of M in Eq. (28) varies between -1.54 and -1.74. The value of N in the equation is independent of the value of y_0^+ used.

[47] An alternative way to define the friction coefficient (on the inner cylinder) is $c_f = \tau_w/(\frac{1}{2}\rho v^2) = [(1-\eta)^2/(\pi\eta^2)]G/R^2$, where v is taken as the velocity of the inner cylinder; on the outer cylinder $c_f = [(1-\eta)^2/\pi]G/R^2$.

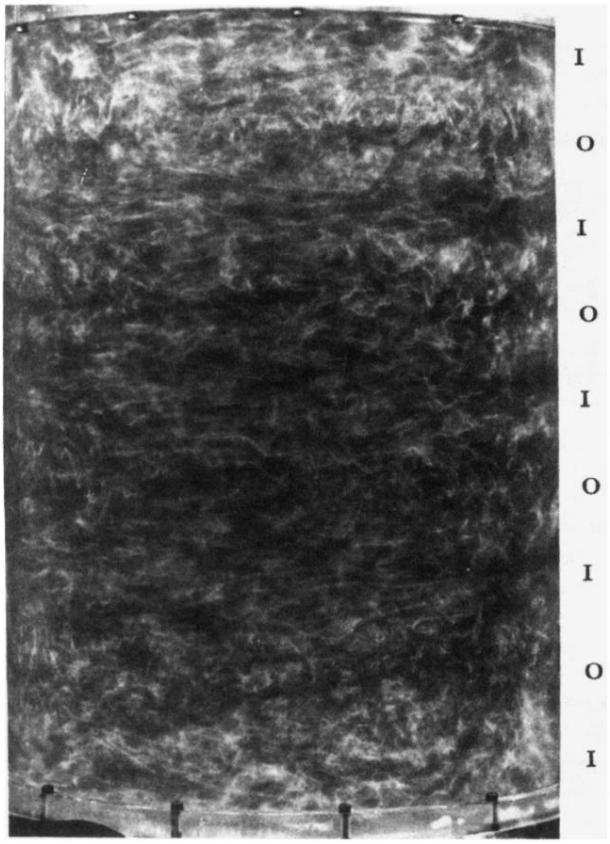

FIG. 1. Flow visualization showing turbulent Taylor vortices at $R = 12\,000$, obtained using a 0.1% concentration of Kalliroscope added to the working fluid. The inflow (I) and outflow (O) boundaries are labeled.

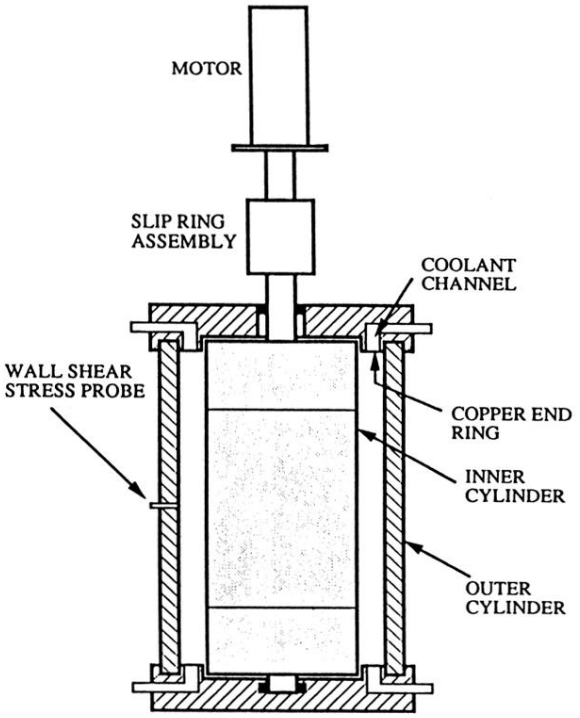

FIG. 2. The Couette-Taylor system consists of a Plexiglas outer cylinder and a stainless steel inner cylinder (see Fig. 3). Temperature control is achieved via coolant channels in each end, separated from the working fluid by thin copper rings.

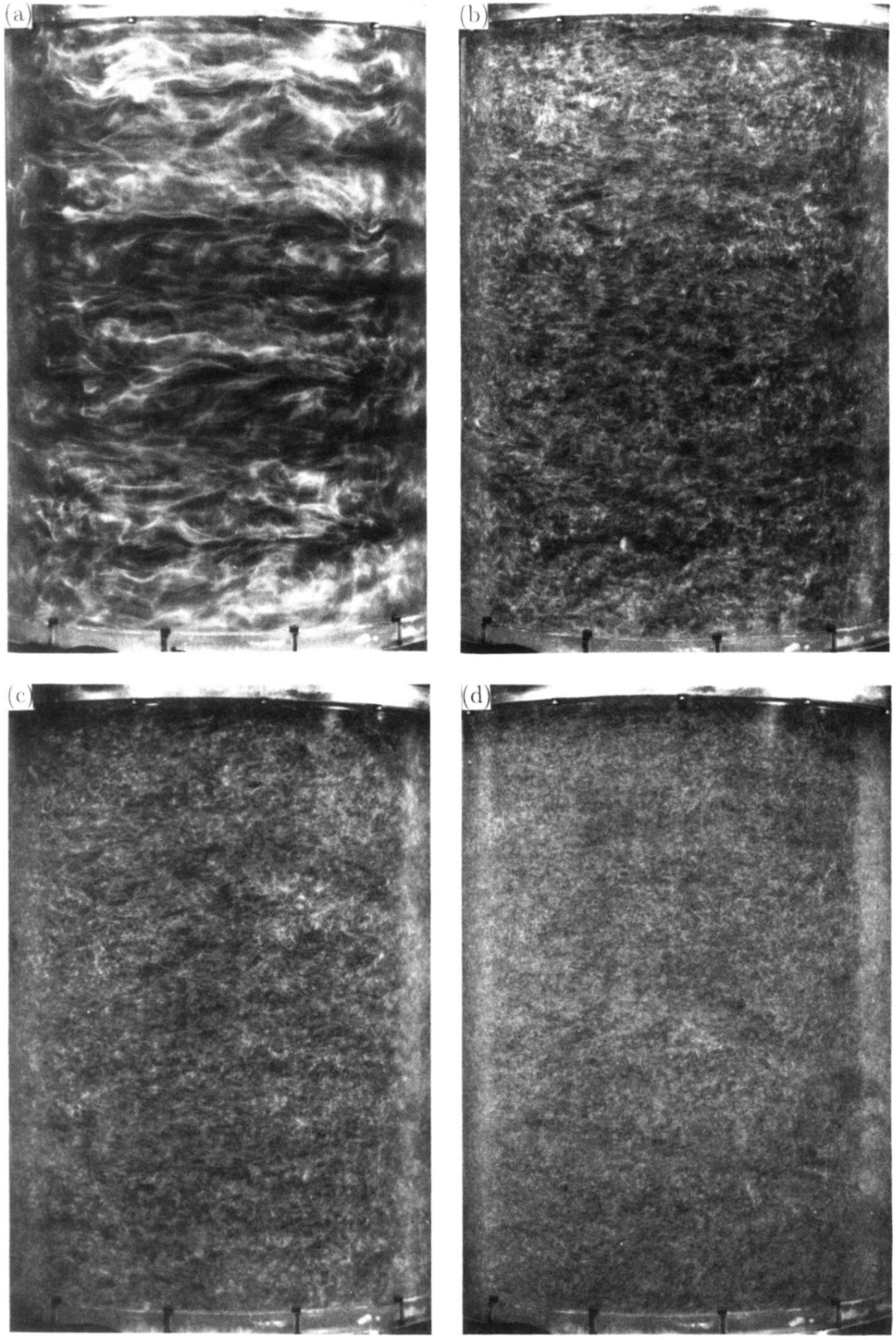

FIG. 5. Photographs of flow states at (a) $R = 6000$, (b) $R = 24\,000$, (c) $R = 48\,000$, and (d) $R = 122\,000$, obtained using Kalliroscope flow visualization. Eight vortices are visible in (a) and (b) and possibly (c), but not in (d).